DEEP

Innovation for:
De-Risking Enhanced
Geothermal Energy Projects

Deliverable

D1.1 Reservoir evolution: Efficacy of coupled surface and downhole monitoring technologies

Report information	
Work package	WP1: Innovation in Imaging and Monitoring Technologies for EGS
Lead	EOST
Authors	Rémi Fiori, EOST; Jean Schmittbuhl, EOST
Reviewers	Peidong Shi
Approval	[Management Board]
Status	Final
Dissemination level	Public
Will the data supporting this document be made open access?	Yes
If No Open Access, provide reasons	[]
Delivery deadline	31.05.2024
Submission date	06.06.2024
Intranet path	DOCUMENTS/DELIVERABLES/Deliverable1.1.pdf

DEEP Project Office | ETH Department of Earth Sciences
Sonneggstr. 5, 8092 Zurich | deep-office@sed.ethz.ch | www.deepgeothermal.org

This project has been subsidized through the Cofund GEOTHERMICA, which is supported by the European Union's HORIZON 2020 programme for research, technological development and demonstration under grant agreement No 731117.

Table of contents

Summary

Initially, the objective of the work linked to this deliverable was to assess the efficacy of coupled surface and downhole monitoring technologies, through the analysis of a reservoir evolution over the course of the DEEP project. To this end, it was planned to deploy a dense surface network in the Soultz-sous-Forêts region and to analyze the acquired data together with downhole measurements in deep boreholes, during a period of active induced seismicity. As it turned out that no downhole monitoring could be done in neither Soultz-sous-Forêts nor Strasbourg areas, the focus has been put on the development and test of new surface monitoring techniques. The concept consisted in deploying small seismic arrays of geophones for induced seismicity monitoring. First, the case study of Strasbourg was considered to offer an alternative approach of studying the induced seismic sequence occurring after GeoVen EGS project shut-in (Georhin, Vendenheim, France) using the DENSAR pool of nodes from Strasbourg University. The choice of instruments and network geometry was justified by the easiness of deployment, even in urban contexts, but also the ability it should give to increase the sensibility to smallest induced earthquakes and to assess the local ambient noise. This report presents the work realized through the PhD project of Rémi Fiori, funded by the French Agency of the Environment and Mastery of Energy (ADEME) and the University of Strasbourg (Unistra) as a support for the DEEP project. The methodology proposed to analyze the post shut-in seismic activity of GeoVen EGS project using array processing techniques is presented (Fiori et al, 2023). The second chosen case study is the FORGE site (Utah) where preliminary results of the application of this methodology have been obtained using seismic arrays with other geometries and deployed by the University of Utah to see how surface monitoring can compare and be complementary to downhole monitoring during the hydraulic stimulation of April 2022.

1. Monitoring seismicity after the Vendenheim shut-in using arrays

This section is a synthesis of the work published in Fiori et al. 2023 (figures are extracted from it) but also an extension of it using other geometries of arrays. **We present the methodology used to analyze the seismic activity during the 4 months after the shut-in of GeoVen project, based on array processing with relatively small seismic arrays.**

1.1 Context and deployment

The GeoVen, EGS project (Vendenheim, France) is an interesting study-case regarding the induced seismic sequence it caused (see Terrier et al, 2022). This seismic activity began in early 2018 and with the first operations on site. It is characterized by more than 580 detected induced earthquakes until end 2022 (22 with MLv > 2 and Mmax = 3.9), distributed into two clearly distinct clusters (Schmittbuhl et al, 2021). The catalog of the whole period was obtained by the BCSF-Renass using template matching techniques on data from the local permanent network. It has a magnitude of completeness (Mc) of Mlv=0.6 to 1.1 depending on the considered period. In 2020, a sequence of earthquakes develops with notably an MLv 3.6 on 4 December 2020 largely felt by the population. Consequently, the operator was asked to stop all activities on site, and undertook a progressive bleed-off and shut-in, spread from mid-December to 2 January 2021. One goal of the monitoring was to follow the seismic activity after the biggest induced earthquake in this area up to then, during the fluid pressure decrease typical of a shut-in. The geophone seismic array approach was chosen as the quickest temporary network to implement while allowing a better sensitivity to the tiniest seismicity, compared to the permanent network already in place (e.g. Schimmel and Gallart 2007, Dean and Sweeney 2019, Karplus and Schmandt 2018)(see 1.2). This sensitivity is essential to have the most complete catalog, which could be a useful contribution for a better understanding of the spatio-temporal interactions between the two clusters, and of the building up of the seismicity leading major earthquakes.

The spatio-temporal evolution of the seismic sequence, obtained with the permanent local network, is summed up in *Figure 1*. For more details on the Vendenheim seismic sequence, see Schmittbuhl et al. 2021.

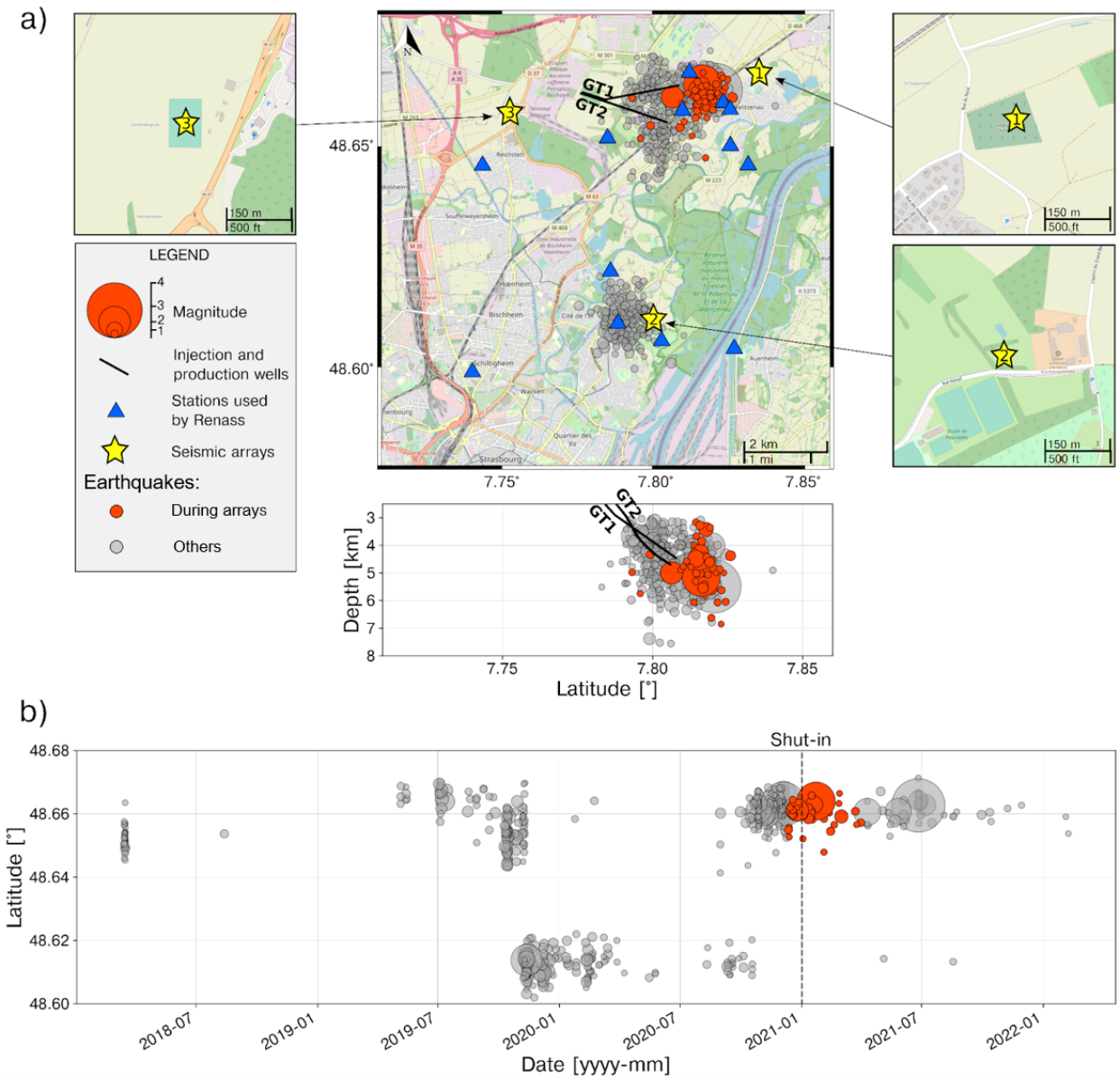

Figure 1: (a) Map of the Strasbourg Eurometropole area, with seismic array locations (the yellow stars), in the vicinity of the two seismic clusters recorded by the BCSF-Renass with the existing network (the blue triangles) operated since mid-2018. The two thick black lines are the production well (GT1) and injection well (GT2). The depth cross section shown under the map is for the seismicity of the northern cluster only. (b) Timeline of the whole seismic sequence until 1 July 2022 (gray) and in particular during the four months of acquisition with seismic arrays (red). The gray vertical dashed line represents the start of the progressive shut-in.

Figure 1 also shows the monitoring network in place before the deployment of the arrays, constituted of permanent seismometers, semi-permanent Raspberry Shakes geophones and seismometers, but also stations made available by the operator temporary after earthquakes exceeding MLv=2. We deployed 3 seismic arrays around the active seismicity area, forming a triangle that ensures an optimal azimuth coverage, at an epicentral distance chosen to be far enough to constrain the depth, but not too far because of sensibility limitations due to the strong anthropogenic noise in such an urban area. The deployment took place as soon as possible after the major event MLv 3.6 of December 4, 2020 (10 December) and was named Densgeoven.

The use of 3-components IGU-16HR SmartSolo geophones (as ‘nodes’) of the DENSAR pool (Strasbourg University), made it quick and easy to deploy. Once on the field, after instrumental parametrization, the only need is to dig a hole of about 50 cm deep, put the sensor inside it, orient to the North, and fill the hole with dirt / rock mixture, for good coupling to the ground and discretion. A counterpart of this kind of instrument is the non-real-time data, saved in a memory

card but not transferred continuously, and the need to swap the sensors every 30 days, when the battery is close to empty. The system requires manpower and cannot be acquiring for a long time without maintenance. So, we decided to put to an end to the deployment when the seismicity recorded by the permanent network was getting less and less active (in terms of rate and magnitude).

We choose small seismic arrays to make it fit in a single field (the seismic array 1-3 in figure 1a) to limit the number of land authorization needed. The geometry of concentric circles and its dimensions, shown in *Figure 2a*, were chosen to allow spatial filtering in a wide range of wavenumbers (*Figure 2b*) without resolution limitation nor aliasing. *Figure 2c* illustrates the admitted boundaries to those effects in the frequency / apparent velocity domain (see Fiori et al. 2023 for more information). To set the most suited dimension to our goal, one must consider the expected frequency content of typical induced earthquakes in this area, considering their depth and epicentral distance, but also the ambient noise content to filter as much as possible in frequency. The higher the number of sensors per patch, the higher the gain in Signal over Noise Ratio (SNR), estimated to $N^{0.5}$ for a patch of N sensors. Here, we constituted arrays of 21 sensors, limited by the pool availability at this time.

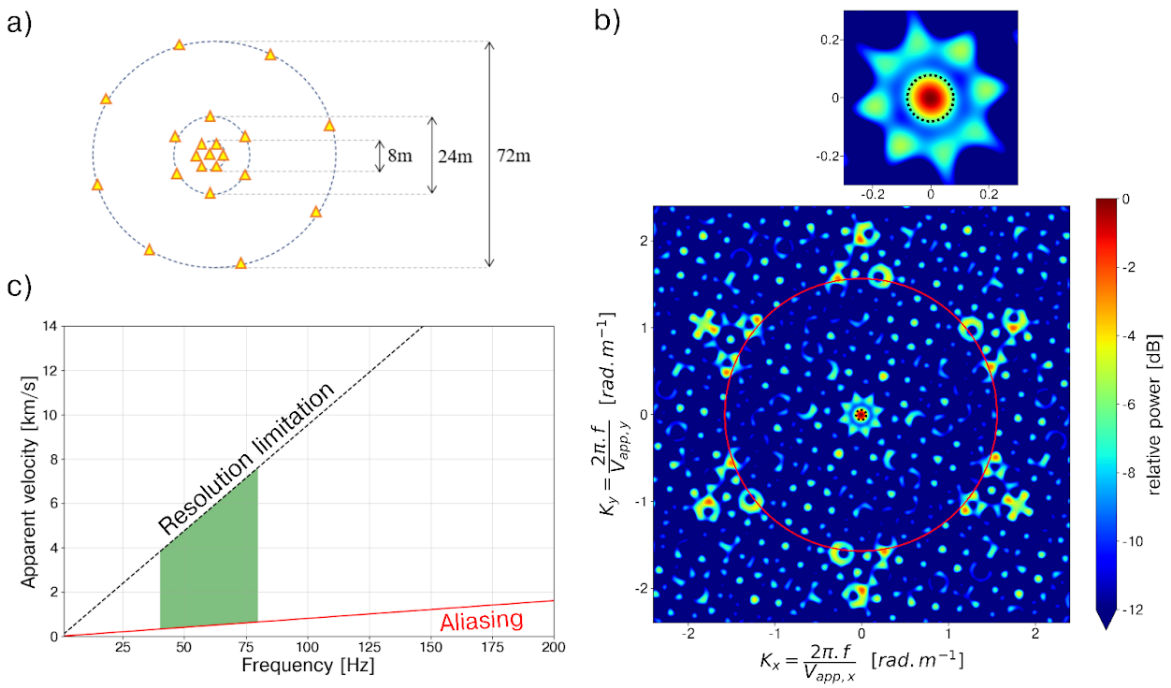

Figure 2: (a) Sensor configuration (yellow triangles) within each of the three arrays and (b) theoretical array transfer function normalized by its maximum, in the wavenumber domain, for the array configuration shown in a). The insert shown at the top is a magnification of the central part of the lower figure. The dashed black circle delineates the resolution limit and the red circle delineates the aliasing limit. (c) Resolution and aliasing boundaries in the frequency-velocity domain. The green area corresponds to the 40–80 Hz interval used in this study.

Regarding the data completeness, only a few sensors did not initialize properly during the deployment, leading to a loss of data during the 30 days corresponding shift. We recovered more than 98% of the total data.

1.2 Noise characterization

To choose the best frequency interval to monitor the seismicity, we analyzed the noise frequency content over time by computing Power Spectral Densities (PSD). *Figure 3a* shows PSDs computed at the central node of the northeast array over the whole period of deployment. We observed a typical anthropogenic noise signature around 10 Hz, with a strong daily and weekly periodicity shown in *Figure 3b*. These periodicities are explained by the working hours, being during daytime and weekdays. The smaller and/or closer the earthquakes, the higher the

frequency range within which energy arrived at the surface (discussed in 1.3). In particular here, we could afford to filter the signal content between 40 and 80 Hz to get rid of much anthropogenic noise while conserving significant seismic signal.

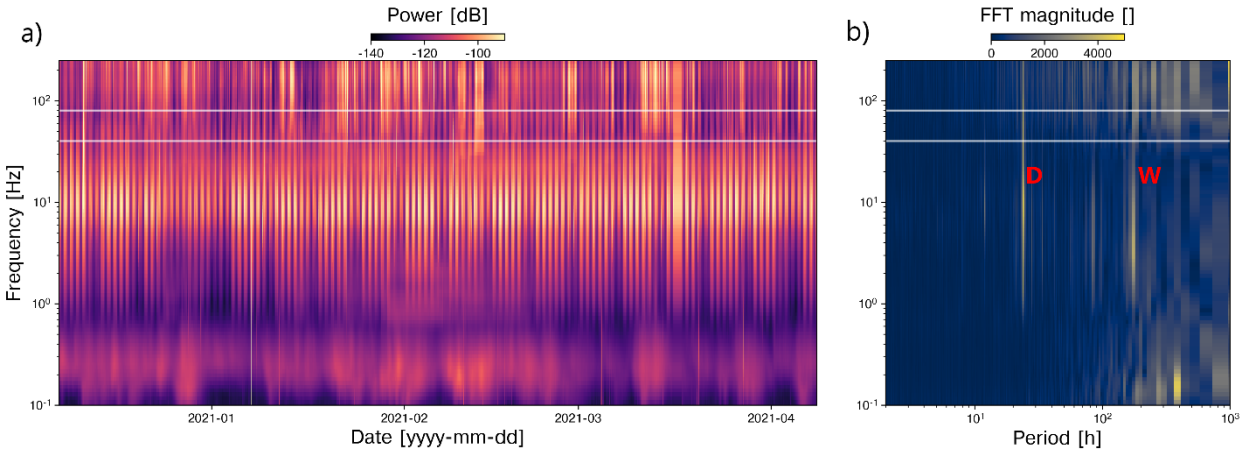

Figure 3: (a) Spectrograms of the PSD computed on vertical traces of the central station of array 1 over the four-month period of acquisition and (b) module of the FFT of the PSD time series for each frequency. The white lines delimit the 40–80 Hz frequency range. Here, D and W red labels refer to the peaks at 24 and 168 h, respectively.

We further characterized the ambient noise by applying a beamforming technique on sliding windows continuously over the 4 months. This kind of array processing consists in computing the azimuth and apparent velocity that better explains the observed wave in terms of energy. We proceeded with a function available in the ObsPy library (Bartlett beamformer), modified to make a grid search in a regular grid in the azimuth and apparent slowness domain. *Figure 4* shows the typical evolution of the best backazimuth / apparent slowness value in each time window for by far the most recurrent and preponderant patterns we noticed in the ambient noise. They are attributed to road vehicles (*a*) or train (*b*). The color corresponds the relative beamforming power, corresponding to the ratio between the energy of the shifted stack (according to the BAZ / apparent slowness) and the autocorrelation.

We modelled the expected azimuthal time evolution of a wave emitted by a train, while it is moving on the railway, considering the speed limitation in this portion of railway. The model has a very similar time evolution as the one recorded computed by beamforming, which supports the fact that these waves are surface waves, travelling rather horizontally at a speed of around 300 m/s.

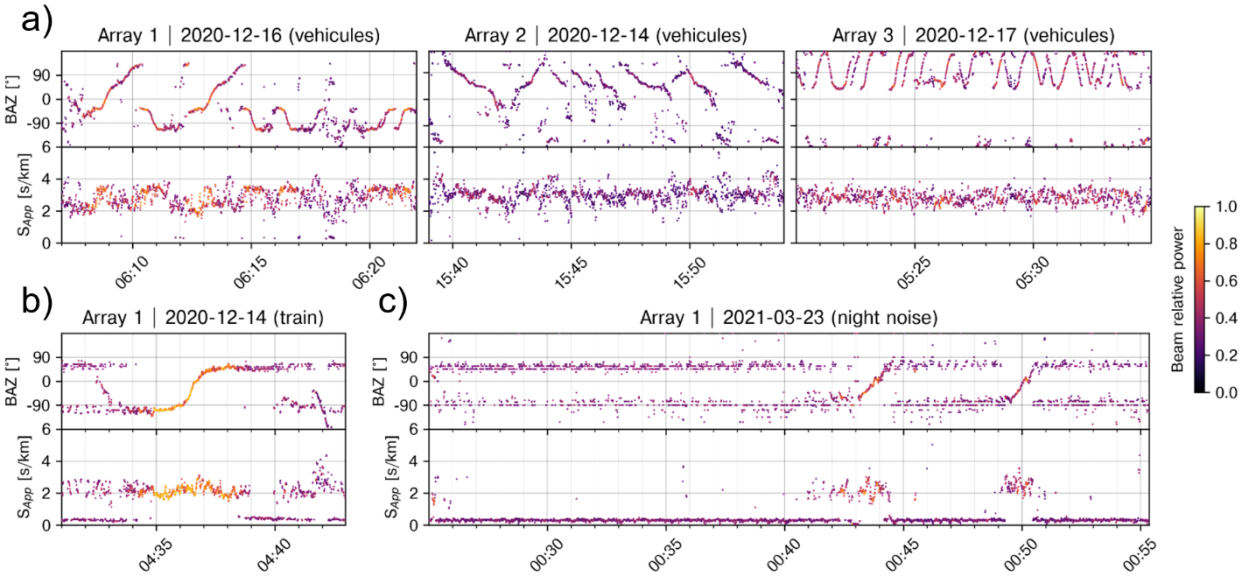

Figure 4: Evolution of the dominant back azimuth and apparent slowness with time, obtained by a beamforming technique on sliding time windows of 1 s after filtering between 5 and 80 Hz (the first line). Typical signature of (a) road traffic during the daytime, (b) a train passage, and (c) noise recorded at night.

1.3 Ambient noise level lowering

In addition to noise characterization, we estimated the median power spectrum of induced earthquakes in this region. We computed PSD on narrow time windows (0.5 to 2s) around the P wave of known earthquakes. The green lines in *Figure 5* represent the median spectrum for 3 different magnitude intervals. In parallel, we computed the Probabilistic Power Spectral Density (PPSD) at the central sensor of the northeast array (blue line and area are respectively the median and 10-90 percentiles). The median noise level at this sensor is close to the theoretical High Noise model. When we confront the earthquakes spectra to the PPSD of the single node, we see that the best SNR for earthquakes of magnitude around 0.5 is between 40 and 80 Hz (shift between the green dotted line and the blue or red solid line), comforting our choice of frequency band for the filtering.

Figure 5 also shows the PPSD of the signal obtained by stacking all the sensors of an array (red line and area). We clearly see the beneficial effect of stacking, that significantly decreases the noise level, especially above the anthropogenic noise level peak around 10 Hz, previously discussed. This reduction is consistent with the estimation of SNR gain by $N^{0.5}$ when stacking N signals containing purely random noise.

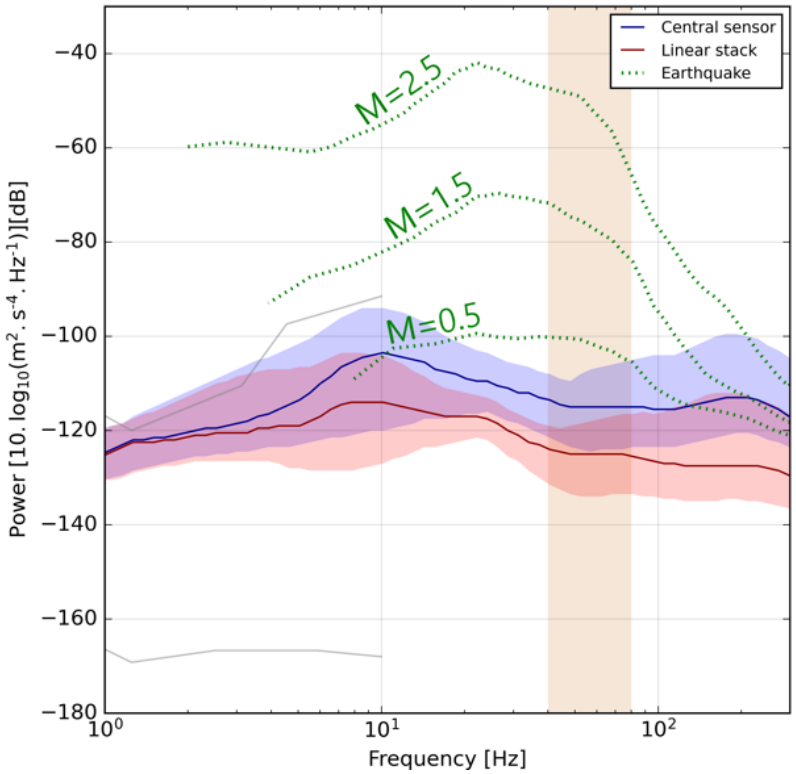

Figure 5: Comparison of the noise level from data at the central station (blue) and from linearly stacked data (red) of the northeast array. The solid line stands for the median of the set of computed PSDs whereas the transparent areas are delimited by the 10th and 90th percentile. The dashed green lines are the PSD of local earthquakes by magnitude. The gray solid lines correspond to the new low-noise model (NLNM) and NHNM (Peterson 1993; McNamara and Buland 2004). The light brown rectangle corresponds to the 40–80 Hz frequency range.

A last point to consider before working in this frequency band are the technical specifications of these sensors. In this case, they are perfectly suited for high frequency analysis, as they have a corner frequency of 5 Hz, with a plateau up to Nyquist frequency, and a sampling rate up to 4 kHz (we choose 1 kHz for this study).

1.4 Detection and location techniques

To detect the seismicity occurring during the 4 months, we first bandpass filter the signal between 40 and 80 Hz. Then, we stack all the sensors of each array to increase the SNR even more and detect events with a classical Short-Term overs Long-Term average (STA/LTA). Although linear stacking already allows a significant increase of the SNR, as shown in *Figure 5*, we rather used a non-linear stacking approach, called Phase-Weighted Stacking (PWS, Schimmel and Paulssen 1997; Thurber et al. 2014). This method consists in weighting the traces with a dynamic factor that evaluates the phase coherency of all the signal (nodes) for each time sample $s_j(t)$ of the $N = 21$ individual traces

$$g(t) = \frac{1}{N}\sum_{j=1}^{N=21} s_j(t)\left|\frac{1}{N}\sum_{k=1}^{N=21}\exp[i\Phi_k(t)]\right|^{\nu} = \frac{1}{N}\sum_{j=1}^{N=21} s_j(t).C(t), \quad (1)$$

where $\Phi_k(t)$ is the instantaneous phase (Bracewell, 1965) of the analytical signal of the trace $s_j(t)$ evaluated at time t. The power ν controls the weight of the phase in the stack ($\nu = 0$ being the linear case). This stacking approach happened to be very efficient in terms of noise reduction in our case, even if we do not relatively delay the traces before stacking. The reason is that the stations are close one to another, and the seismic wave coming from a typical induced earthquake is coming with a rather vertical incidence, in comparison to the mostly horizontally propagating surface noise. *Figure 6* illustrates the effect of such a stack in a period containing a small earthquake of magnitude -0.4 (using $\nu = 3$) and some significant noise around it.

We decided to try and locate only the events detected in the same time window at the three arrays. We follow this conservative approach to avoid false detections, due to coherent noise being recorded simultaneously at two arrays. This can especially happen because of the small size of the arrays.

To locate events, we use a Matched Field Processing (MFP) method. It consists in first, computing the Bartlett beam signal of each array, in a band window containing a given seismic phase of an earthquake, and projecting the beam in a 3D space using a velocity model. Then, we compare it to the theoretical beam obtained for a given source coordinate, and we obtain a pseudo probability of presence of the source to be at this given coordinate (Baggeroer et al. 1993). We look for the maximum value of this presence probability through a grid search to obtain the most probable position of the source, given the velocity model. In our case, we compute the beamforming of all the arrays independently, and combine them afterwards, instead of computing them on a same time window. It allows to isolate smaller time windows, which happened to be more performant when dealing with small earthquakes and noise (see Fiori et al. 2023 for more details). After obtaining this first set of earthquakes, we estimate the average arrival time delay between sensors within each array and recompute an improved PWS after delaying the traces accordingly, to detect a few more earthquakes.

Finally, we estimate the local magnitude using the P peak value on the PWS trace directly, and the distance to the hypocenter. Fiori et al. 2023 justifies this estimation on PWS rather than individual traces by comparing these estimations to those of the BCSF-Renass. Our observations suggest that the important ambient noise level seems to impact the estimations from BCSF-Renass, making them saturate for lowest magnitudes.

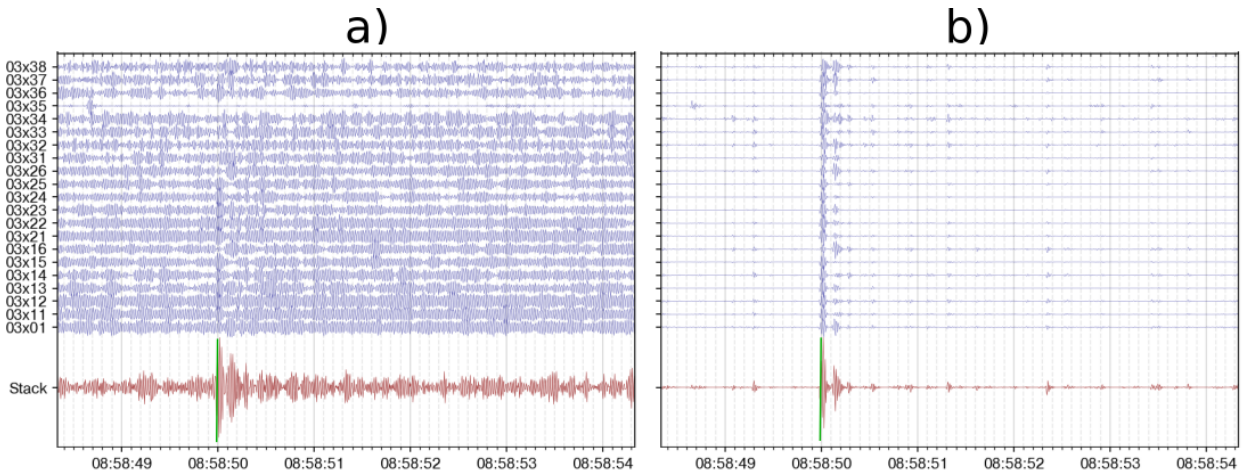

Figure 6: Illustration of the effect of the linear and phase-weighted stack, on a magnitude −0.4 earthquake (13 December 2020), at the northwest array. The blue lines correspond to individual station vertical component and the red lines correspond to the summation of them; (a) traces band-pass filtered between 40 and 80 Hz and (b) traces filtered and multiplied by the coherency term C(t) defined in equation 1. Green solid vertical lines indicate the detection time.

Figure 7 shows a chart of the whole workflow. A cluster analysis has been performed also, but is not shown in this report (see Fiori et al 2023).

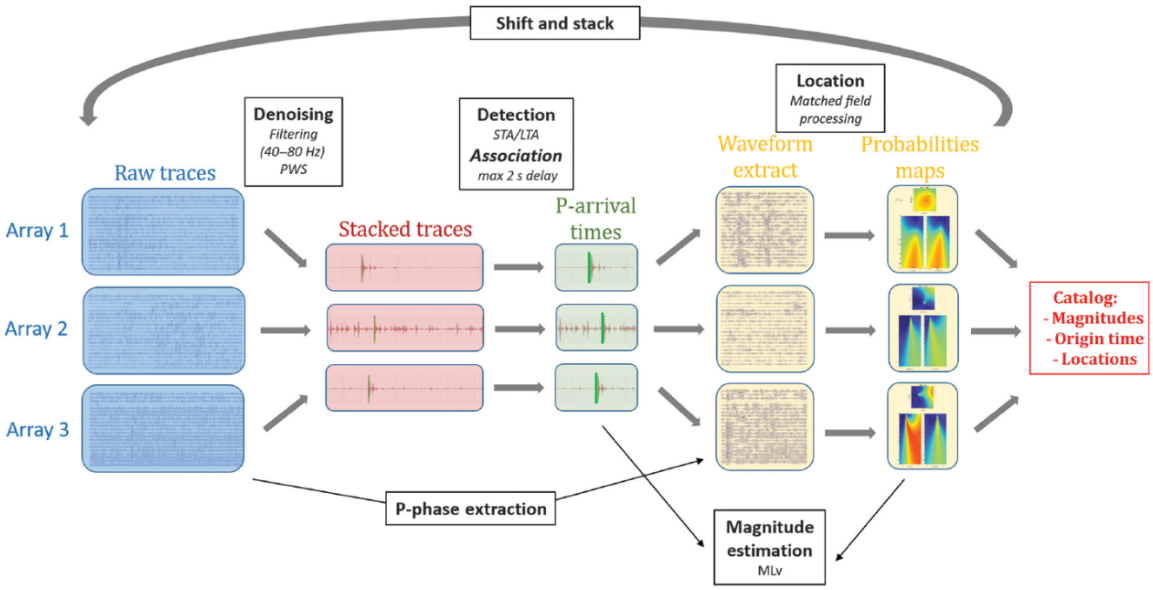

Figure 7: Chart of the whole data process, from raw data acquisition to seismic catalog.

1.5 Seismicity analysis

Our worklow allows us to successfully locate 216 events, corresponding to 86% of the events left after the association at three arrays (*Figure 8*). This represents more than four times more events than in the reference catalog. Most of the events of the present catalog are located within or close to the northern cluster (the blue-filled ellipse). Despite not using the same velocity model as the BCSF-Renass, we observe a similar depth distribution of the events centered at approximately a 5 km depth, which is close to the depth of the wells (4.5 km). To estimate the error made on the horizontal epicenter locations, we compute the dispersion of the location probability (or coherence) maps. We approximate the coherence function as a 3D Gaussian function around the maximum value, of which we determine the standard deviation. This standard deviation is approximately 600 m on average. In addition, we use as a reference the relative relocation obtained by double differences by Schmittbuhl et al. (2021), whose relative location error has been estimated to be a few tens of meters. All the relocated hypocenters are gathered close to

one another. By assuming no shift between the barycenter of the relocated events and the barycenter of the events located by MFP, the average distance between the hypocenters gives an approximation of the error made with the array processing location. The localization precision of the MFP to locate events in the targeted area is similar to the precision of the BCSF-Renass (approximately 1 km according to Schmittbuhl et al., 2021). Our catalog reveals three events in the southern cluster whereas the reference BCSF-Renass catalog does not show any event in this area during this four-month period. We manually checked the waveforms and relative delays between the three arrays for these events to confirm that they were actually located in this southern cluster. For the largest ones, we were able to observe a faint signal at some stations from the permanent network and locate it roughly in the same area by a traditional phase-picking approach, thanks to stations used by the BCSF-Renass close to the southern cluster (see *Figure 1*). This observation could mean that there is still an active connection between the northern cluster and the southern cluster, even after the injection is stopped.

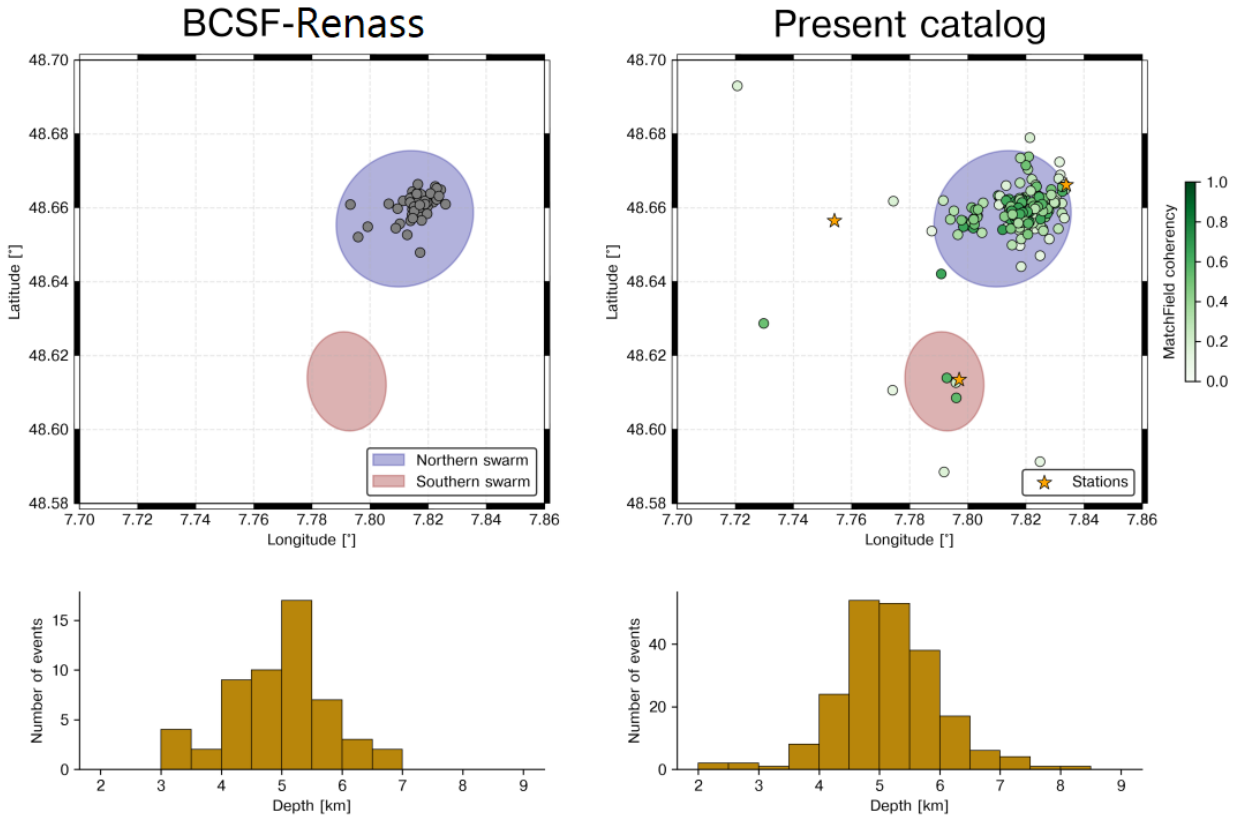

Figure 8: Comparison of the induced earthquake locations for the four-month period from (a and c) the BCSF-Renass French institute catalog and (b and d) the present catalog built using arrays. (a and b) Maps of the epicenters. The areas where the seismicity occurred during the whole induced seismic sequence are roughly drawn in blue and red color. The stars show the array's location. The orange color scale of scatter markers refers to the maximum probability found with the MFP. (c and d) Depth distribution.

Figure 9b shows the magnitude-time distribution of the events located by MFP. According to our magnitude estimation, most of the newly detected events are of lower magnitude than the ones in the reference catalog. The distribution of the number of events per magnitude bins follows a Gutenberg-Richter law (Gutenberg and Richter, 1944) (*Figure 9c*), which gives credit to the magnitude estimation from PWS stacks. We estimate a b-value of 0.62 ± 0.03 based on the algorithm proposed by Ogata and Katsura (1993), which is consistent with the b-value of 0.60 ± 0.44 computed for the reference catalog for the same period, also using array peak amplitudes. However, the b-value estimated on our catalog has a much lower uncertainty due to the higher number of low-magnitude events. We estimated a lowering of the magnitude of completeness from 0.3 to −0.5 with our approach. The overall seismicity rate (shown in *Figure 9a*) is decreasing with time during the four months, especially after the shut-in. However, we notice periods of

higher density of events in our catalog, which are not observed in the reference catalog. This is particularly the case around 12 December 2020 and 25 December 2020 and around 3 January 2021. These bursts of seismic activity are not associated with observable changes in the fluid pressure at the GT2 wellhead, which is smoothly decreasing with time following the shut-in (*Figure 9*). The fact that these periods of more intense earthquake activity are not observed in the reference catalog, which has a higher magnitude of completeness, means that the b-value evolves temporally, and is higher (in absolute value) during these bursts. The first burst occurs at the very beginning of the installation period of the three arrays (10 December 2020) following the strong MLv3.6 induced event of 4 December 2020. The observed increase in the small seismicity rate from 10 December to 12 December and its stop on 15 December indicate that the temporal distribution of seismicity does not follow a traditional Omori law. The second and quite intense burst, which begins on 25 December, follows an MLv2.1 event and exhibits a time evolution of the seismic rate that is more typical of an aftershock sequence. On the contrary, the MLv2.8 earthquake of 22 January, the largest event during our experiment, has significantly fewer aftershocks. Moreover, during the few days before and after this event — approximately between 12 January and 3 February — we observe a deficit of small-magnitude earthquakes.

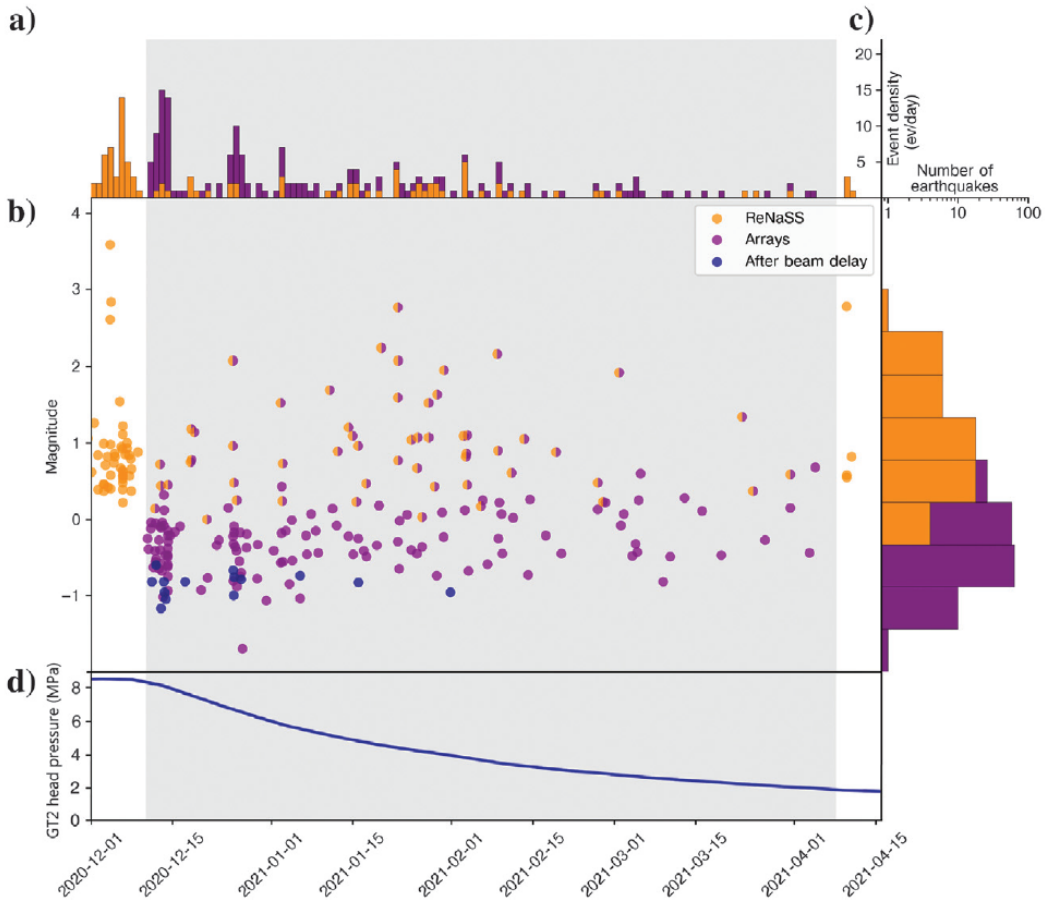

Figure 9: (a) Histogram of the event density per day on the whole period; (b) magnitude-time distribution of events of the reference and the present catalog (orange and purple, respectively) from 1 December 2020 to 15 April 2021, where the gray area stands for the four month period of acquisition (from 12 December 2020 to 8 April 2021); (c) histogram of the number of earthquakes per magnitude bin for the period in gray; and (d) GT2 wellhead pressure evolution during the bleed-off and shut-in of the well (modified after Terrier et al., 2022).

1.6 Exploring other array geometries

As previously shown, the seismic activity reduced significantly with the decrease of fluid pressure induced by the shut-in of December 2020. The seismic rate and maximum magnitude decreased, with no more MLv > 2.0 after 1.5 months and no more MLv > 1.0 after 3.5 months. So, we decided to remove the seismic patches and end the first deployment. However, a few days after removing

the sensor, a MLv2.8 occurred, followed by a MLv2.7, 1.5 month after, and eventually a MLv3.9 the 26 of June 2021. This earthquake, occurring 6 months after the beginning of shut-in, happened to be the biggest of all the sequence, and was largely felt by the population. In reaction, we decided to deploy a new seismic array network, to follow the post main shock activity and improve the understanding of its triggering process.

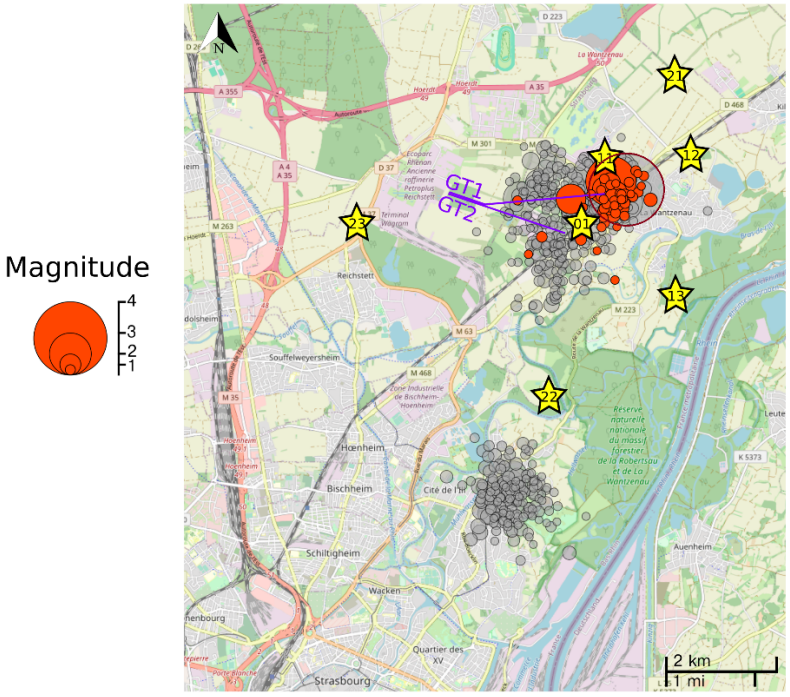

Figure 10: Same background map (and seismic sequence represented) with the new seismic array set-up. The purple circle corresponds to the MLv3.9 earthquake.

We also use the opportunity to test different network geometries compared to the first deployment (Densgeoven 2). We spread 87 sensors over 7 seismic arrays (*Figure 10*), with 3 typical shapes: big or small spiral, and one cross (*Figure 11a*). We keep one array closer to the Southern cluster, to have a better sensitivity to the seismicity occurring there, and easily distinguish from where the earthquakes are coming. We tried to cover the azimuth of the Northern cluster homogeneously and placed arrays 23 and 13 such that we better constrain potential seismicity occurring in between the two mains clusters. Also, we used the same sites as during the first deployment for arrays 23 and 12, to make it possible in the future to compare the two different array geometries, even if they were operating at different time (meaning under different earthquakes and noise conditions).

There are mainly 3 advantages of this kind of spiral shape, that we could see on the transfer functions beforehand but wanted to test in practice. First, we can orient the spiral in such a way that the biggest aperture is pointing to the targeted area to monitor (i.e. the cluster), to reduce the central spot of the array response, and so improve the resolution in that same direction. Secondly, this kind of shape uses more space in typical rectangle shaped field than concentric circles (we can play with the width/length ratio). Finally, the amplification spots are certainly more numerous in the transfer functions than for concentric circles, but they are also more homogeneously spread in the wavenumber 2D space, meaning that we are less likely to obtain a strongly biased result when applying a beamforming to find the best BAZ / apparent velocity couple for a given incoming wave (*Figure 11b*).

Due to the important number of sensors, we set the frequency rate to 500 Hz for this deployment (for storage and post-acquisition processing cost). This is a lesson learnt from the past

deployment because we observed that the frequency content of typical induced earthquakes here does not contain much energy above 100 Hz.

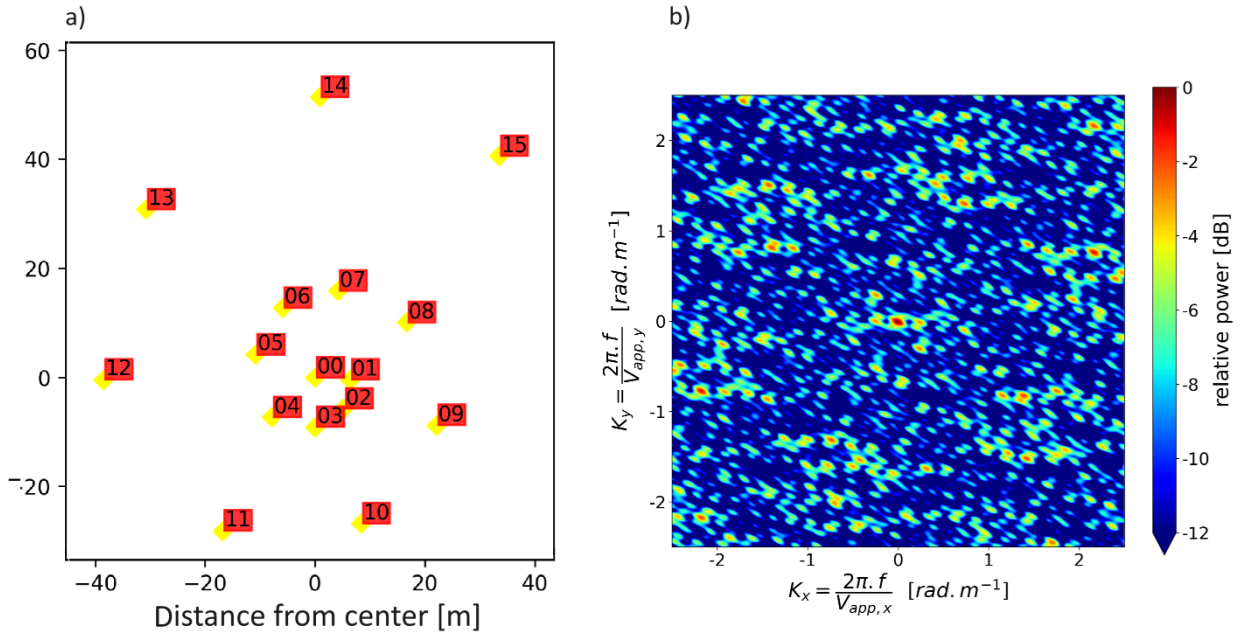

Figure 11: (a) Typical shape of the 'big spiral' arrays (adapted to the shape of the deployment field) (b) corresponding theoretical transfer function.

The recovered data completeness is a bit less than for the first deployment (~96%) for two mains new reasons: one of the sensors has been dug up, and one other has been cemented by building workers, due to works in the Wantzenau cemetery that we were not aware of.

Like on the data of the first deployment, we proceed to beamforming on time window sliding continuously on the whole period of acquisition. We observe similar patterns, especially at site 23, common to the first deployment. *Figure 12* is summing up the noise characterization by beamforming at all the arrays, for two distinct frequency/apparent slowness bands (4-20Hz in *Figure12a* and 40-80Hz in *Figure 12b*). We made normalized 2D-histograms weighted by the relative beamforming energy, for each hour of the day, and represented in the figure the most representative hours for daytime noise. Changing the frequency band affects the apparent velocity that can be observed,because arrays are acting as wavenumber filters. The higher the frequency band, the smaller the apparent slowness that can be analyzed without resolution limitation.

As previously said, construction work was operated on site 12 (Wantzenau cemetery) during the whole deployment, highly impacting the noise analysis, especially during daytime where we have most of the other anthropogenic noise we aim to analyze. We only sometimes observe the truck and train passing nearby. Interestingly, on other arrays, the predominant noise comes from various sources, depending on the frequency band used. For instance, most of the noise energy on array 23 is coming from the nearby expressway for lower frequencies (roads in yellow on the background map) while it is coming from the highway in higher frequency band. Site 13 also seems to be mostly affected by surrounding forest roads, although the patterns are less clear. Another identified strong source of noise for several arrays (01, 11 and even 22) is the Arlanxeo rubber factory (golden square marker on both maps), especially between 4 and 20 Hz. The energy radiated by the train along the railway is dominating at array 01 between 40 and 80 Hz, while its typical signature is usually around 5-20 Hz.

The principal sources of energy recorded at array 22 have not been identified, although it could be interesting to have a further look at the beamforming results at this array, especially because

this array seems to have a convenient position to investigate potential transient signals between the Northern and Southern cluster, that could explain the mechanism that connect them.

As we apply the exact same process as during first deployment, the noise highlighted between 40 and 80 Hz is the one that impacts the most the monitoring performances of the network.

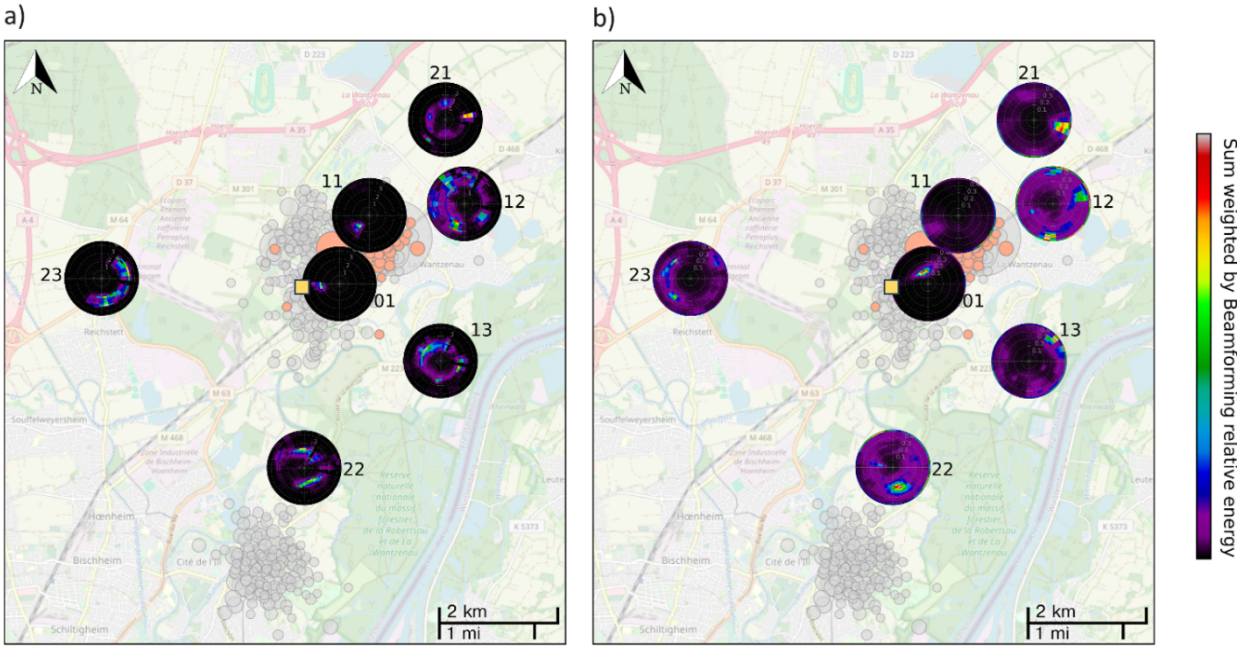

Figure 12: Maps with radial 2D histograms of the backazimuth / apparent slowness computed on sliding time windows of length chosen to contain at least 10 wavelengths of the smaller frequency in the band. The sum value at each bin is weighted by the beamforming relative energy, as previously defined. We bandpass filter between a) 4-20 Hz and 0.55-4 s/km b) 40-80 Hz and 0.01-0.4 s/km

After applying the same process as during the first nodal deployment, we obtain the catalog shown in *Figure 13*. The seismic rate and maximum magnitude drop significantly faster after MLv3.9 of June 2021 than after the MLv3.6 of December 2020, and we record only one earthquake of vertical local magnitude over 1. Like during the first deployment, the seismicity is particularly active after the main shock (at the very beginning of the deployment period). We did not perform cluster analysis on these data, unlike for the first deployment. We note that the Southern cluster showed a bit of activity, with one earthquake even recorded by the permanent network.

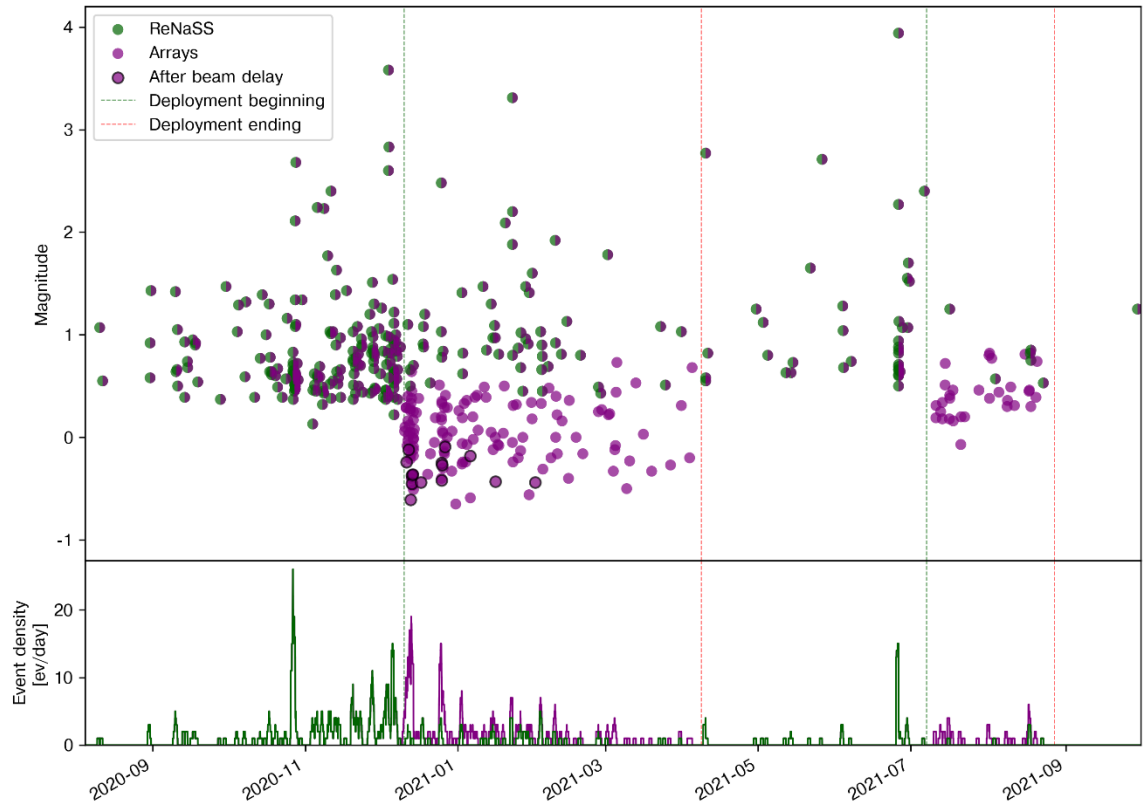

Figure 13: Summary timeline of the seismicity recorded during the two arrays deployments a) time magnitude representation b) smoothed seismic rate

2. Monitoring of FORGE stimulation

We applied and further developed our seismic arrays methodology on the dataset acquired by Utah university during the FORGE stimulation of April 2022. The idea was to evaluate it in a different context: with a main noise source of natural origin, during stimulation, and with a different network geometry. Also, not only a 1D velocity model was available for this area. A final reason was the existence of two other seismic catalogs of this stimulation, which could be compared to ours. One was done by the University of Utah, using only surface station. The other is the high-resolution reference catalog, obtained by GeoEnergie Swiss using a combination of borehole stations and Distributed Acoustic Sensing (DAS).

The following work has been possible thanks to the collaboration within the DEEP project, with Gesa Peterson, Peter Niemz and Claudia Finger, among others. We had constructive discussions, and they provided the waveform data and 3D velocity models used in this work. Here are the preliminary results.

2.1 Context

Hydraulic stimulation of the 16A(78)-32 production well was carried out from April 16 to 22, 2022. This consisted of 3 injection phases: first at the end of the drilled well, in the “open hole”, then others upstream during phases 2 and 3, injecting through holes perforating the casing. The main objective of the seismic monitoring was to map the fracture network resulting from stimulation with sufficient accuracy to define the best direction in which to sink the 16B(78)-32 production well to maximize the probability of connection with the injection well. The aim was also to assess the associated risk and to test algorithms and procedures for traffic light systems, as well as to test the performance of certain instruments in real-life conditions.

During hydraulic stimulations, geochain stations (a chain of several geophones linked together) were not continuously operational at depth due to high temperatures. Because of this technical failure, the composition of the monitoring network fluctuated over the 3 stimulation stages, causing a variation in terms of catalog resolution.

In this section, we focus on phase 3, for which the GES reference seismic catalog obtained has the best localization resolution. During this phase, they acquired data from a geochain in 58-32 and a two-level analog channel in 56-32 at reservoir depth (2535 m), a geochain in 78B-32 (down to 1890 m), DAS data in 78B-32 and 78-32, and the BOSS (Borehole Optical Seismic System) tool in 78-32.

A preliminary version of the high-resolution seismic catalog obtained by GES was published on July 30, 2022 (https://doi.org/10.15121/1879450), for which some of the earthquakes were examined visually, followed by a revised version on October 11, 2023 (https://doi.org/10.31905/52CC4QZB) including the localization of smaller, automatically detected seismic events, a correction of magnitude estimates and the removal of some duplicate events (see *Figure 14*).

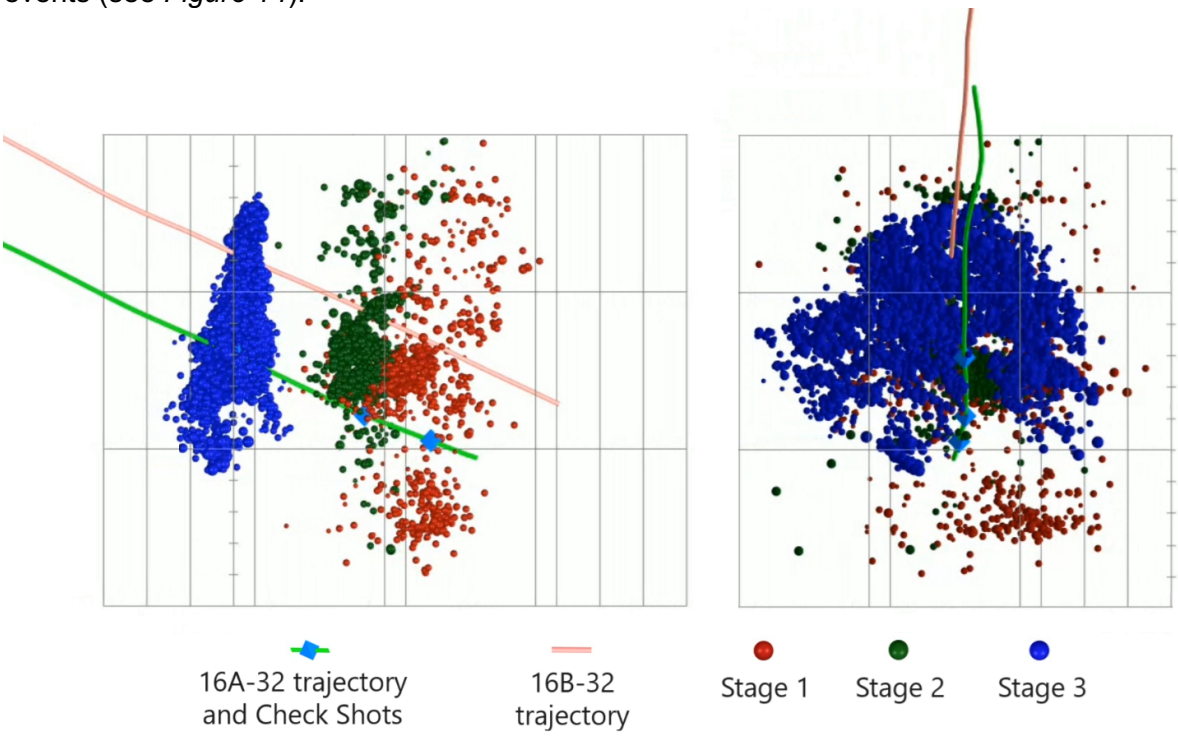

Figure 14: Final version of the high resolution seismic catalog obtained by GES using data from borehole stations (geochains, BOSS and DAS), covering the 3 stimulation stages.

During these stimulations, 13 surface arrays composed of 16 3C-SmartSolo geophones were operating at 500 Hz. They had been deployed on sites such that they provided homogeneous azimuthal covering around the termination of well 16A, where most of the seismicity was expected because of the stimulation (*Figure15*).

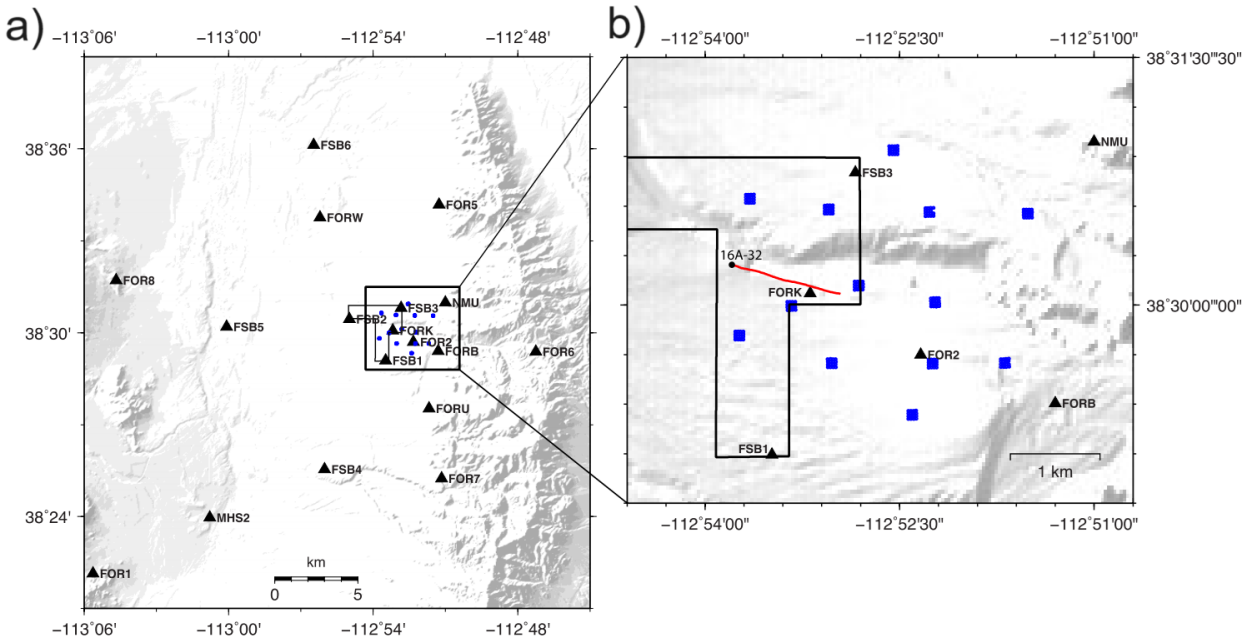

Figure 15: Topological map with the surface seismic array deployment of April 2022 a) at the scale of the regional permanent seismic network (black triangles) b) zoomed around FORGE site (delimited by black solid lines) with the stimulated well trajectory in red and the surface geophones in blue (surface arrays forming squares). Extracted from Whidden et al. (2023).

The geometry of each array is a regular square 4x4 grid with 30 m horizontally and vertically between each node. The array response of such geometries is composed of regularly spaced amplification lobes of theoretically maximum amplitude, leading to total aliasing for the wavenumbers at each peak. *Figure 16* shows the real array response after deployment of one of the arrays, zooming onto the central lobe on *Figure 16a* and showing the same wavenumber boundaries as for Densgeoven. In comparison, the central spot is smaller because of the bigger aperture, but the aliasing lobes are stronger and close from each other. This leads to a optimal frequency band (without aliasing at apparent velocities typical in the context) that is of lower frequency (*Figure 16c*).

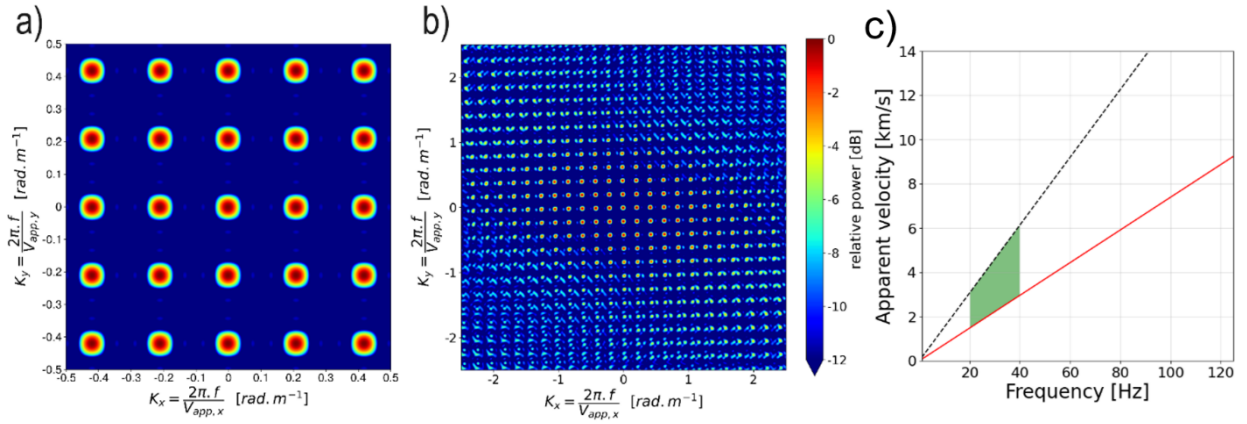

Figure 16: a) and b) Array transfer function of one of the seismic array, at two different scales c) Conversion to the frequency / apparent velocity domain.

2.2 Data and quality control

The data acquired by the seismic surface array are made available by the University of Utah by online request. It represents a few Tbytes in total. We downloaded via this server but report here some technical problems we encountered while working with it.

First, no metadata is available, which is important in particular when looking for acquisition time periods and instrumental responses. The data are piecewise complete over time, while the 30

days of acquisition correspond to the typical autonomy of these instruments and there had been no sensor swap explaining those occasional lack of data. The data gaps are random, and not the same within the same array. Also, for at least the first and last day of acquisitions (but sometimes more), the value of the signal is a constant that seems to correspond to the maximum or minimal value that can be digitized by the instrument (clipping behavior).

Finally, the most concerning issue we encountered is that the instrumental response seems to vary over time, as if the amplification factor was changed during acquisition. *Figure 17* illustrates this issue: we computed PPSD after building metadata files, using the technical specification from the company selling the sensors and the parameters that were used. We can clearly see the median ambient noise being shifted during some periods of time. We make sure that it is not explained by punctual changes in the ambient noise by looking at the most stable PSD, around 3 Hz. These changes are in the order of 20 dB, and are observed randomly over the period, but always exactly at midnight. The most probable explanation for these observations is incorrect post-acquisition processing when moving the data to the server. We gave these feedbacks to the University of Utah.

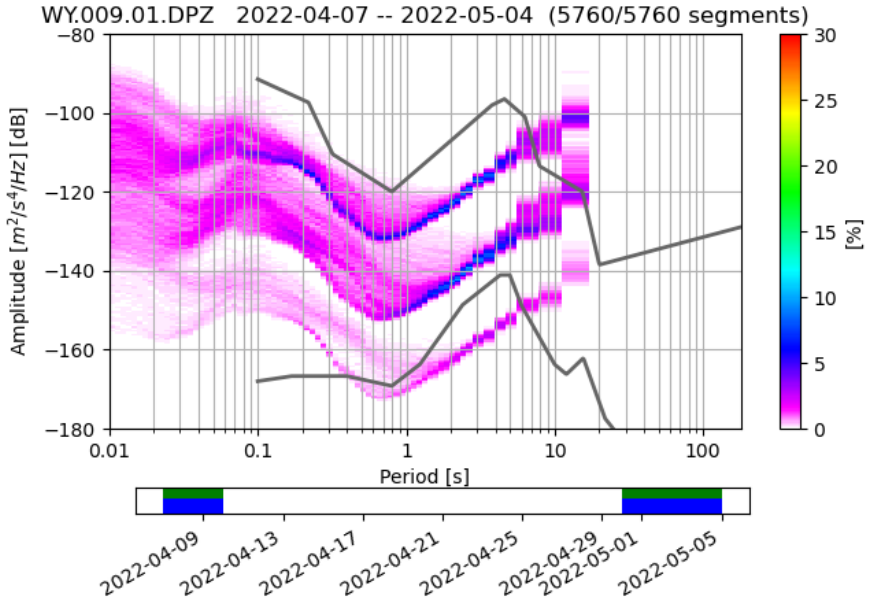

Figure 17: (top) PPSD computed on time slices of 75 s of sensor 9 of array 1 (bottom) time completion over the whole period of acquisition.

The data we used for testing our monitoring methodology has been sent directly by Gesa Peterson and Peter Niemz. It does not contain the artefacts previously discussed. To make it possible to share with us, despite a low upload rate on their side, the data are only covering the 3 most intensive hours of stage 3 in terms of seismic activity.

2.3 Noise characterization

Although the data available through the online link contain instrumental responses artefacts, we manually corrected them by deconvolving the signal with a different instrumental response during each day, according to the shift of ~20 dB observed on initial PSD. We obtain a timeseries of PSD over time, which is continuous for some stations with no data gap. *Figure 18* shows these PSDs. The noise nature is different from the one measured around Vendenheim, with no clear periodicity linked to anthropogenic activities in the PSDs. We put this in parallel with the wind speed recorded at the closest weather station, located in the airport of Milford around 14 miles away from FORGE site (data downloaded from free access buffer of the National Centers for Environmental Information www.ncei.noaa.gov). We notice an important correlation between the wind speed at the ground level and the amplitude of the ambient noise PSD. This was expected

because of the important temperature variations in this region (causing frequent wind burst), and because it is desertic, so the sensors are not hidden from the wind. Phase 3 of the stimulation happened during the second most windy and noisy day of the month, making the conditions relatively bad for surface monitoring. The noise correlated to the wind is particularly important in high frequency bands, for which the seismic arrays were designed.

We wanted to compare these PSDs computed from surface measurements with downhole data, available online as well, from BOSS and Geochain tools. We could not make it because the metadata were not available, and we did not know the response curve so we could not build instrumental response ourselves.

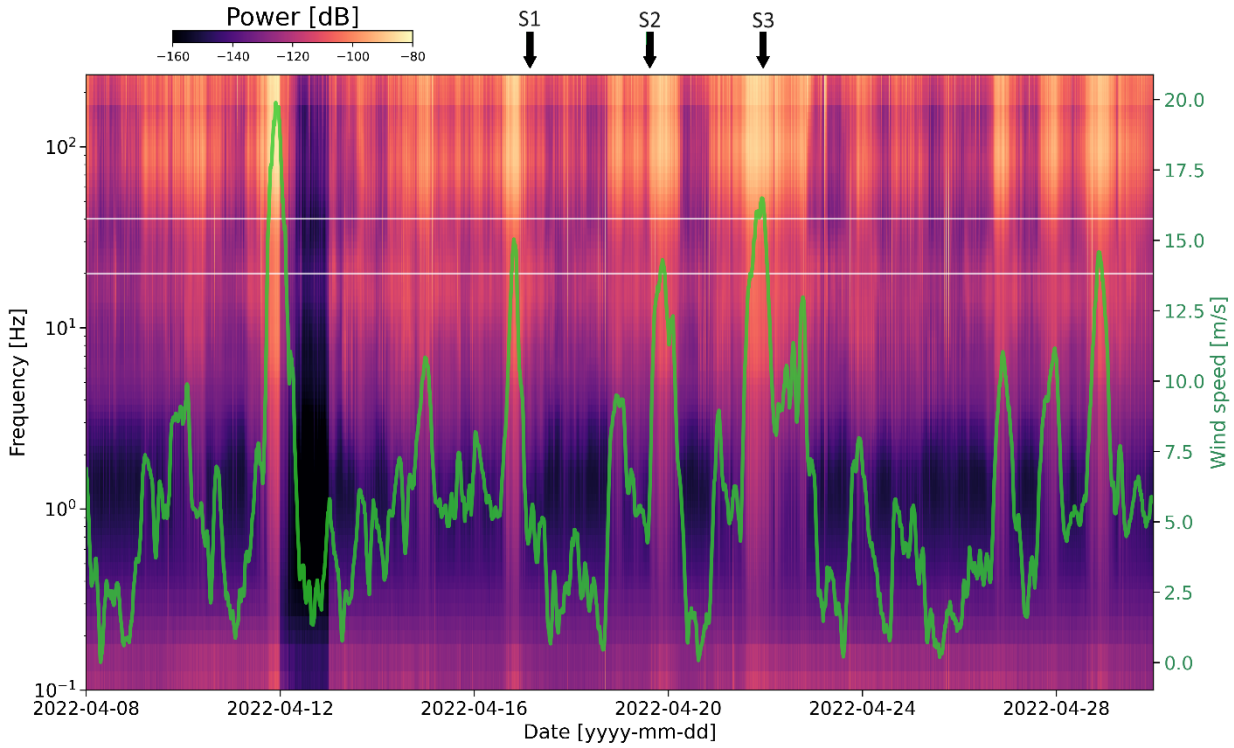

Figure 18: timeseries of PSD computed on a surface geophone over the whole period of deployment; green solid line represents the wind speed at the ground level, measured at the closest weather station (located in Milford airport). The label above arrows correspond to the periods of stimulation phases.

Besides, we measure a significant ambient noise level difference between each array site. This implies that choosing a 3-arrays triangle configuration like in Vendenheim would require a preliminary noise assessment of each candidate site. The number of detected events on the nosiest sites is significantly smaller than for other sites.

2.4 Novelties in the processing

We filter the signal between 20 and 40 Hz to adapt the processing to the noise conditions and arrays geometries. We also adapt the STA/LTA detection threshold.

To cope with the relatively high seismic rate (up to 1 event per second triggered downhole), in comparison to shut-in periods, we consider the travel time from source to array center when associating the triggers at each array. Each event is then associated to the corresponding earthquake of the GES catalog, with the reasonable (and checked) assumption that the GES catalog did not miss any earthquake detected at the surface. We don't consider the unassociated detections in the following.

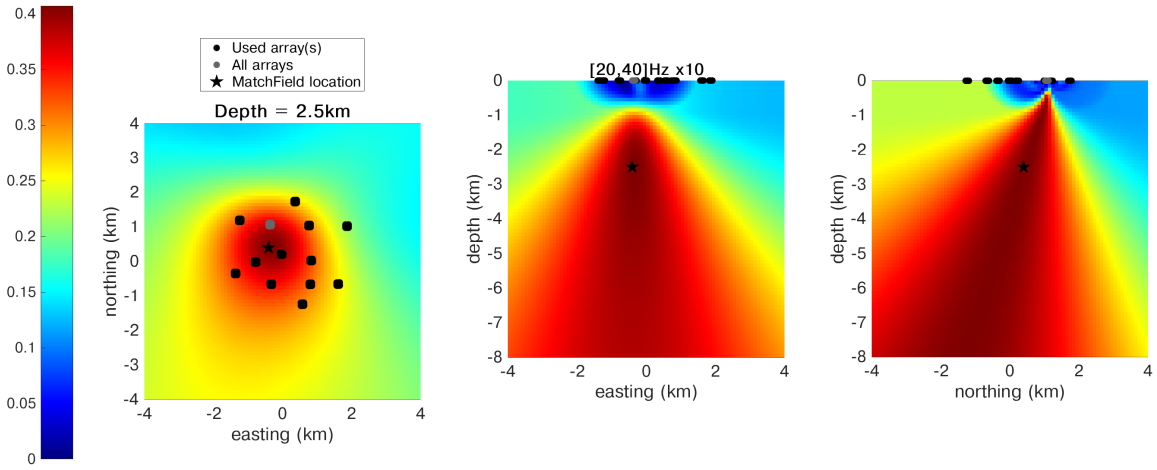

Figure 19: Slices of probability of presence map, at the maximum coherency value, obtained using only the array in gray, a 1D velocity model and a time window centered on S-wave, for an earthquake of Mw -0.4.

The main defaults of the processing done on DENSGEOVEN (discussed in section 1) was the use of only P-wave, and not S-wave. Although they generally contribute in better constraining the location, their lower frequencies were much impacted by the anthropogenic ambient noise, which made it difficult to use them with MFP. Also, we wanted to test to apply MFP on the stacks of each seismic array, considering the whole network as a big array. This could allow to add the lost information about time delay between arrays, missing because we are proceeding to MFP on individual arrays on separated time windows.

For this purpose, on this new dataset, we compute MFP on the P-wave (vertical component) but also on the S-wave (transverse component, obtained after rotation according to the location given by GES catalog) at 20-40 Hz. *Figure 19* shows the probability map for a Mw -0.4 earthquake, obtained with MFP on a P-wave with the 1D velocity model. We also compute MFP on the raw linear stacks of each array (for P and S-wave), at 0.5-2 Hz, to avoid aliasing corresponding to the response of the whole network. Then we weigh the P-wave MFP with the P-wave stack MFP (resp. S-wave) by multiplying them together. Finally, we take the average of the obtained P and S probability map.

We take into account the altitude of sensors, while we considered the ground as plan during Densgeoven deployment.

To identify the P and S-phase, we use the theoretical arrival time obtained with the source time given by GES and the 1D velocity model. *Figure 20* shows an example of the signal for two earthquakes, the biggest of the sequence (Mw 0.13) and a smaller one (Mw -0.89). It illustrates the difficulty to confidently identify the seismic phases for small events, because of intermediate phase and S to P conversion caused by the West-East uprising granite layer. To support the phase identification, we tested a method combining beamforming and polarization, using a code developed and shared by Claudia Finger (Finger et al. 2023), but the identification results were not conclusive even for the biggest earthquakes.

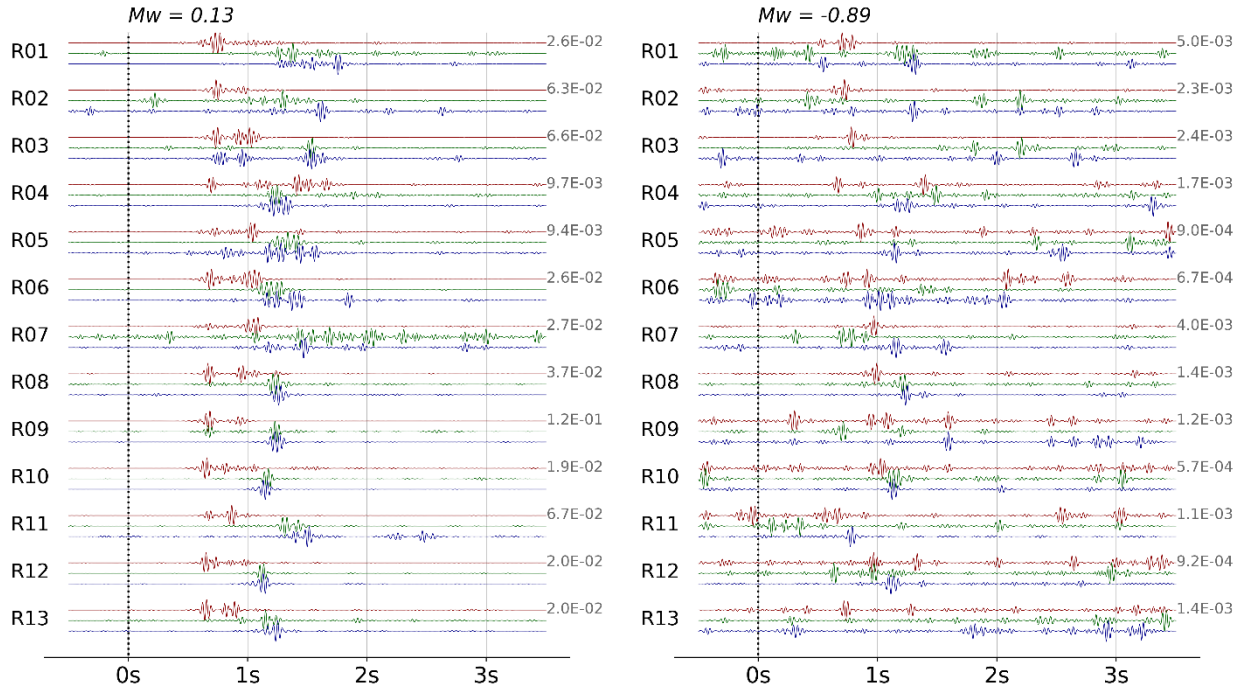

Figure 20: PWS stacks at all 13 arrays, after two events of different magnitudes; red lines are vertical components, blue and green are respectively transverse and radial components; numbers in gray are the scaling factors of the timeseries.

2.5 Comparison of seismic catalogs completeness

Figure 21 shows the detected and associated events, in comparison to the GES catalog. We successfully detected and associated 1.11% of the total seismicity reported in the reference catalog, and 37.38% of the earthquakes above Mw-0.6.

Without going into details here into the observed differences between the first and the last version of GES catalog, we note much more consistency in the magnitude estimation between peak values recorded at the surface and estimated Mw. Nonetheless, we still observe inconsistencies. If we try to estimate the magnitude of completeness (Mc) of both catalogs, based on the repartition curves taken separately, we find about Mw -1.4 for GES catalog and about Mw -0.6 for ours. Our catalog should contain all the events above Mw -0.6 which is not the case when comparing to the reference catalog. This could be explained by an error of magnitude estimation in the reference catalog. Indeed, some of the events of biggest magnitudes are barely visually distinguishable from the noise on the surface data, while being located in the same area as other events clearly seen at the surface. Also, the different network geometry for the surface and downhole networks could introduce bias in the magnitude of completeness..

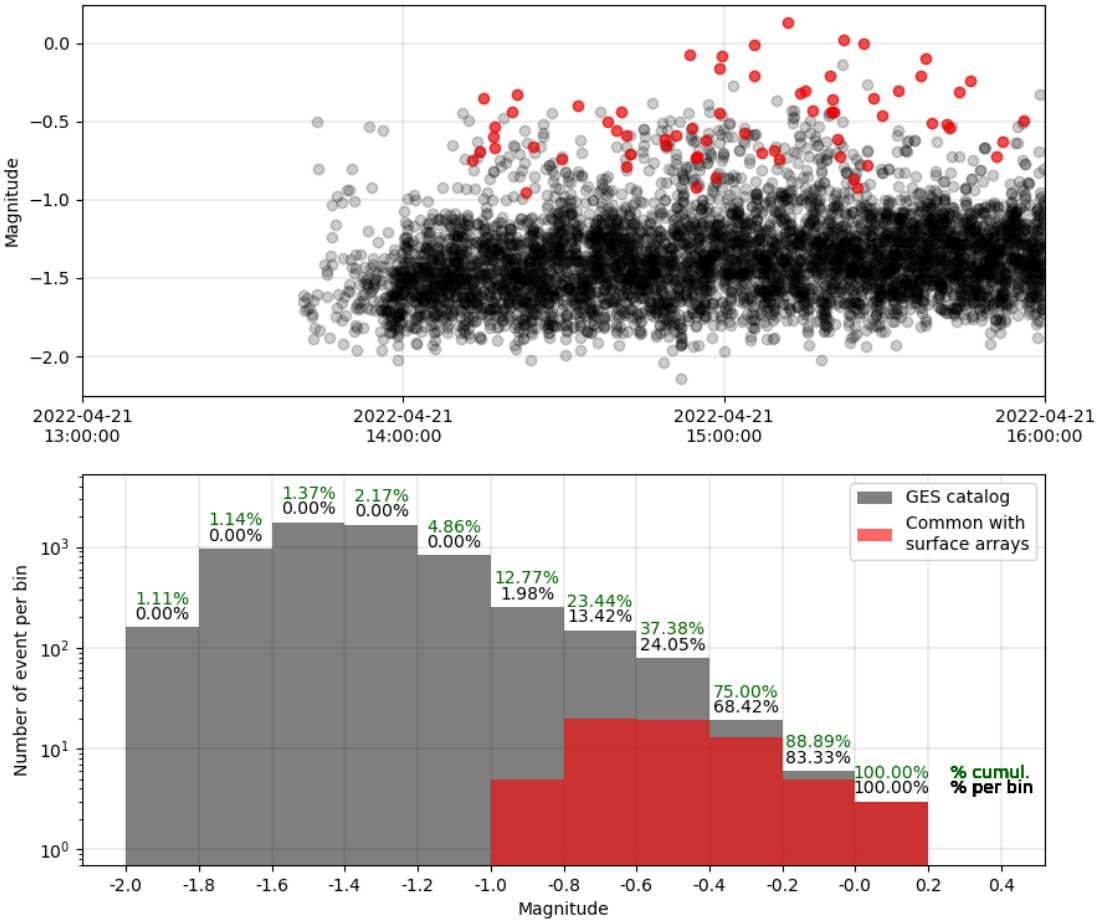

Figure 21: (top) time-magnitude repartition of the seismicity during the 3 first hours of stimulation stage 3; (bottom) magnitude-number distribution on the same period. The written percentages represent the portion of earthquakes in our catalog in comparison to the reference, for each bin (black) and for the cumulative of all bins above (red).

2.6 Impact of 3D velocities models

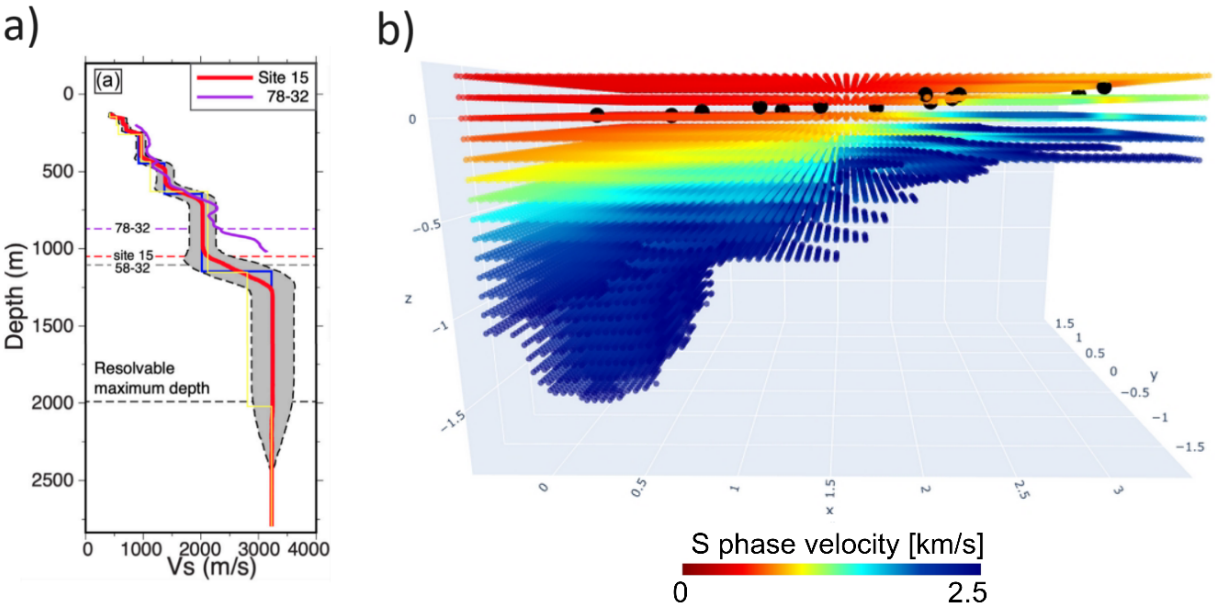

Figure 22: a) 1D velocity model from Zhang and Pankow (2021) for P velocities and Lellouch et al. (2022) for P to S ratio; b) 3D velocity model from Niemz et al. in prep.

We located the detected – associated earthquakes by MFP as described in 1.4, using two different models to compare them. On the one hand, we use an average 1D velocity model extracted from Zhang and Pankow (2021) for P velocities and Lellouch et al. (2022) for P to S ratio (*Figure 22a*). On the other hand, we used a 3D model under construction, shared by Peter Niemz (Niemz et al. in prep) and obtained by smoothing a pseudo 3D model using the travel times at surface arrays (*Figure 22b*). The 3D model is of interest because it takes into account the frank 2D asymmetry of the geology below the surface network.

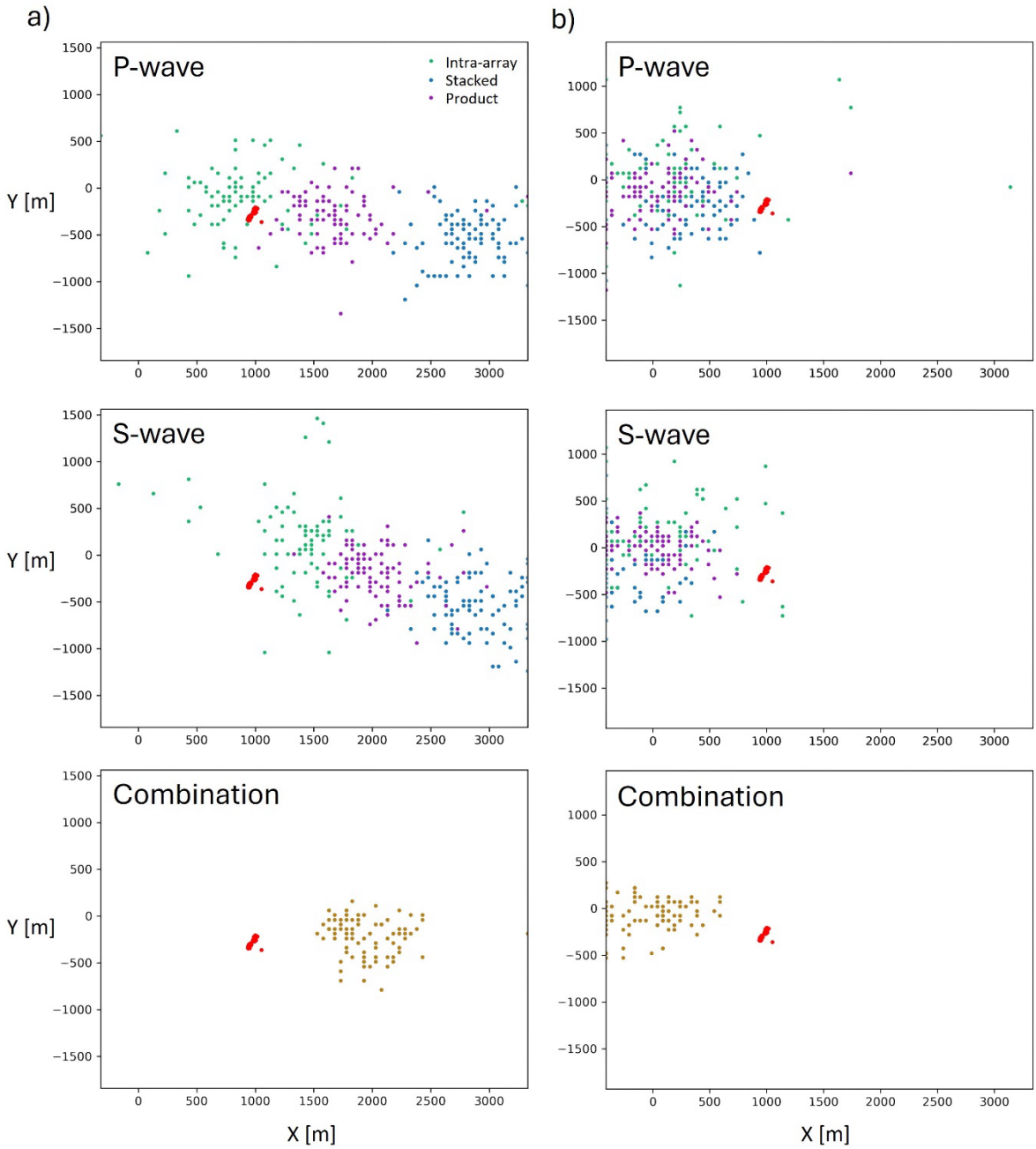

Figure 23: Distribution of the earthquakes locations with a) the 1D velocity model b) the 3D velocity model; green corresponds to the MFP on P (resp. S) seismic phase within each array and combined afterward, like for Densgeoven; blue corresponds to MFP on stacks between arrays; purple is the product of the two MFP for each phase; gold is the average of the purple locations of P and S; red are the locations obtained by GES with downhole monitoring

The preliminary location repartitions are presented in *Figure 23*. The spread of the cluster is much more important for our location than those of the reference catalog, because of the bigger

uncertainty. Globally, the barycenter locations are off-centered by a similar amount in both cases, compared to the reference locations, to the West for the 1D model and for the East for the 3D model (explained by the underestimation of travel times in the 1D velocity model in the eastern region due to shallower granite). Besides, the different uses of MFP give similar results (in terms of cluster barycenter distances) with the 3D model but not for the 1D model. Using only P-waves with a 1D velocity model is what gives the results of least difference with the GES catalog.

These unexpected results have to be discussed with the team who built the 3D velocity and found much better performances of the 3D model over the 1D when locating with full-waveform techniques.

As a last observation, we computed and compared the theoretical travel times with both models, for the events detected by surface arrays (*Figure 24*). Note that the travel time is not increasing with the distance because of the non-plane topography (for the 1D and 3D models) and the 2D asymmetry of the geology (3D model). We compared the modeled arrival times with manual picks of P and S wave for the biggest earthquake of the sequence and found important differences between both picked and computed arrival. From these observations, the 3D velocity model does not seem to better explain the arrival times at surface arrays, which is an abnormal observation because this model was explicitly smoothed to better match those data. In particular, the P-waves seems better explained by the 1D velocity model. Note that the picks shown here might be different from the ones used by Niemz et al. to calibrate their 3D velocity model.

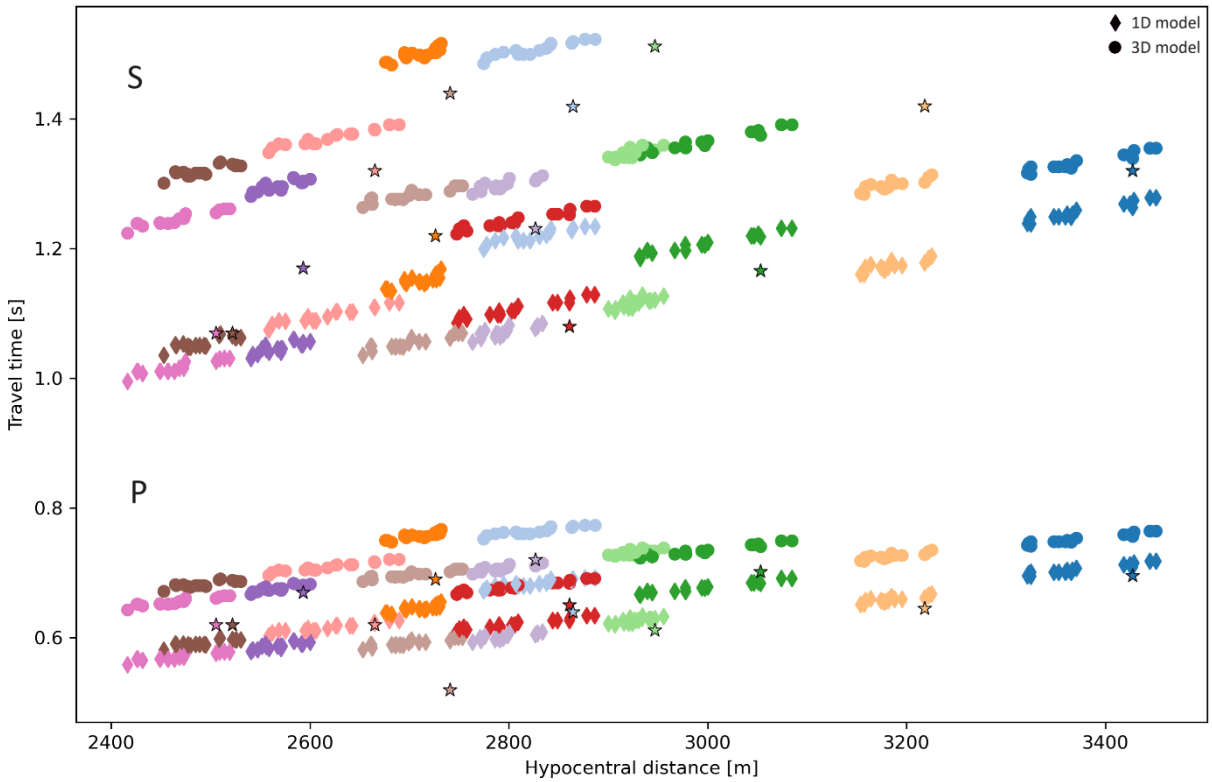

Figure 24: Theoretical arrival times computed for the 56 earthquakes detected on surface arrays with our method, and with GES locations (circles and diamond); each color corresponds to a different array, for P travel times (top) and S travel times (bottom); stars correspond to arrival time deduced from manual picks on stacks.

3. Conclusions

We propose an array processing method with small seismic arrays to monitor induced microseismicity in two contexts: the urban context of Geoven site (Strasbourg, France) and the rural context of the Forge site (Utah, USA). The technique is particularly of interest in the urban context where the strong anthropogenic noise level makes the detection of small events difficult

with standard seismic networks. The design of our arrays allows us to investigate up to high frequencies (40–80 Hz for our the Geoven site and 20-40 Hz for the Forge site) without meeting aliasing problems and to enhance the S/N using a PWS technique. After a STA/LTA detection and association, we automatically locate earthquakes with an MFP approach. We apply this method to the four-month period following the shut-in of the injection in the Georhin wells (Vendenheim, France). We significantly enriched the reference catalog made with the local surface network with five times more earthquakes, lowering the magnitude of completeness by more than half an order of magnitude. Some of these earthquakes have been manually checked by analysts using the permanent network. The higher number of referenced events and the enhanced S/N allow us to have more insight into the subcluster behaviors of low-magnitude events. Our enriched catalog highlights an intermittence of seismic activity in the northern cluster during the period preceding the largest event, although the fluid pressure is decreasing progressively. Also, some activity is revealed in the southern cluster, located 5 km south of the injection well, previously considered as quiescent during this period. Similarly, to what the reference catalog shows for the whole sequence, we do not find any evidence of earthquakes in between the two clusters, which leaves open the question of the mechanisms for stress transfer. For the Forge site, in-depth comparison with the GeoEnergySwiss catalog that includes downhole instrument acquisitions, was performed. We highlight the methodology adaptation needed to process the data, inherent of the surface array geometry, as well as the noise context and higher seismic rate. The surface array data analyzed with the proposed PWS/MFP technique, detect the highest magnitude events (> Mw -0.6) with a recovery of 37% illustrating the high potential of the technique. Locations with the 1D velocity model are actually better than those with the 3D model suggesting that improvements will rely on a more advanced development of the velocity model.

References

Induced and triggered seismicity below the city of Strasbourg, France from November 2019 to January 2021
Schmittbuhl, J., Lambotte, S., Lengliné, O., Grunberg, M., Jund, H., Vergne, J., Cornet, F., Doubre, C., and Masson, F. (2021). Induced and triggered seismicity below the city of Strasbourg, France from November 2019 to January 2021. Comptes Rendus. Géoscience, 353(S1):561–584.

Monitoring induced microseismicity in an urban context using very small seismic arrays: The case study of the Vendenheim EGS project.
Fiori, R., Vergne, J., Schmittbuhl, J., & Zigone, D. (2023). Geophysics, 88(5), WB71-WB87.

BCSF-Rénass
BCSF-Rénass, Bureau central sismologique français - Réseau national de surveillance sismique, https://renass.unistra.fr

Rapport Phase 1 du CE créé en appui à l'administration sur la boucle géothermique GEOVEN: Préfecture du Bas-Rhin, Strasbourg,
Terrier, M., F. De Santis, R. Soliva, B. Valley, D. Bruel, Y. Géraud, and J.Schmittbuhl, 2022, France, 26 avril 2022.

Observation and modeling of seismic background noise
Peterson, J., 1993, U.S. Geol. Surv Tech. Rept. 93-322, 1–95.

High-resolution frequency-wavenumber spectrum analysis
Capon, J., 1967, Proceedings of the IEEE, 57, 1408–1418, doi: 10.1109/PROC.1969.7278.

Ambient noise levels in the continental United States
McNamara, D. E., and R. P. Buland, 2004, Bulletin of the Seismological Society of America, 94, 1517–1527, doi: 10.1785/012003001.

Noise reduction and detection of weak, coherent signals through phase-weighted stacks
Schimmel, M., and H. Paulssen, 1997, Geophysical Journal International, 130, 497–505, doi: 10.1111/j.1365-246X.1997.tb05664.x.

The Fourier transform and its applications
Bracewell, R. N., 1965, McGraw-Hill.

An overview of matched field methods in ocean acoustics
Baggeroer, A., W. Kuperman, and P. Mikhalevsky, 1993, IEEE Journal of Oceanic Engineering, 18, 401–424, doi: 10.1109/48.262292.

Seismic Monitoring of the 2022 Utah FORGE stimulation: The view from the surface.
Whidden, K., G. M. Petersen, and Kristine L. Pankow. *PROCEEDINGS of the 48th Workshop on Geothermal Reservoir Engineering. pp. SGP–TR–224*. 2023.

Wavefield composition analysis from three-component beamforming improves thickness estimates of sedimentary layers
Obiri, E., K. Löer and C. Finger, 2023 : European Association of Geoscientists & Engineers, 84th EAGE Annual Conference & Exhibition, Jun 2023, Volume 2023, p.1 – 5, doi: 10.3997/2214-4609.2023101004

Comparison between distributed acoustic sensing and geophones: Downhole microseismic monitoring of the FORGE geothermal experiment.
Lellouch, Ariel, et al., *Seismological Society of America* 91.6 (2020): 3256-3268.

High-resolution Bayesian spatial autocorrelation (SPAC) quasi-3-D Vs model of Utah FORGE site with a dense geophone array
Zhang, Hao, and Kristine L. Pankow. *Geophysical Journal International* 225.3 (2021): 1605-1615.

Frequency of earthquakes in California.
Gutenberg, Beno, and Charles F. Richter, *Bulletin of the Seismological society of America* 34.4 (1944): 185-188.

Frequency-dependent phase coherence for noise suppression in seismic array data.
Schimmel, Martin, and J. Gallart*, Journal of Geophysical Research: Solid Earth* 112.B4 (2007).

The use of nodal seismic acquisition systems to acquire limited-scale surveys.
Dean, Tim, and Denis Sweeney., *First Break* 37.1 (2019): 55-60.

Preface to the focus section on geophone array seismology.
Karplus, Marianne, and Brandon Schmandt., *Seismological Research Letters* 89.5 (2018): 1597-1600.